

Efficient Broadband Near-Infrared Emission in the GaTaO₄:Cr³⁺ Phosphor

Jiyou Zhong, Ya Zhuo, Fu Du, Hongshi Zhang, Weiren Zhao,* Shihai You, and Jakoah Brgoch*

Efficient broadband near-infrared (NIR) emitting materials with an emission peak centered above 830 nm are crucial for smart NIR spectroscopy-based technologies. However, the development of these materials remains a significant challenge. Herein, a series of design rules rooted in computational methods and empirical crystal-chemical analysis is applied to identify a new Cr³⁺-substituted phosphor. The compound GaTaO₄:Cr³⁺ emerged from this study is based on the material's high structural rigidity, suitable electronic environment, and relatively weak electron–phonon coupling. Irradiating this new phosphor with 460 nm blue light generates a broadband NIR emission ($\lambda_{em,max} = 840$ nm) covering the 700–1100 nm region of the electromagnetic spectrum with a full width at half maximum of 140 nm. The phase has a high internal quantum yield of 91% and excellent thermal stability, maintaining 85% of the room temperature emission intensity at 100 °C. Fabricating a phosphor-converted light-emitting diode device shows that the new compound generates an intense NIR emission (178 mW at 500 mA) with photoelectric efficiency of 6%. This work not only provides a new material that has the potential for next-generation high-power NIR applications but also highlights a set of design rules capable of developing highly efficient long-wavelength broadband NIR materials.

1. Introduction


Broadband near-infrared (NIR) light is playing a more crucial role in food quality testing and analysis, night vision, and

J. Zhong, H. Zhang, W. Zhao
School of Physics and Optoelectronic Engineering
Guangdong University of Technology
Guangzhou 510006, China
E-mail: zwren123@126.com

Y. Zhuo, J. Brgoch
Department of Chemistry
University of Houston
Houston, TX 77204, USA
E-mail: jbrgoch@uh.edu

F. Du
School of Metallurgy and Chemistry Engineering
Jiangxi University of Science and Technology
Ganzhou 341000, China

S. You
College of Materials
Xiamen University
Xiamen 361005, China

 The ORCID identification number(s) for the author(s) of this article can be found under <https://doi.org/10.1002/adom.202101800>.

DOI: 10.1002/adom.202101800

the medical diagnostic fields than ever before.^[1–4] There is a particular focus on materials operating in the 700–1100 nm region of the electromagnetic spectrum because this range covers the characteristic absorption signals of the C–H, O–H, and N–H normal modes. Analyzing these vibrations enables the quick and non-destructive detection of biomolecules, including sugar, protein, fat, or the presence of harmful ingredients like pesticide residues.^[5,6] Moreover, the NIR light in this energy region is known as the first biological window. It allows an appreciable penetration depth in biological tissues, making the NIR light suitable for radioisotope-free tissue imaging and noninvasive blood glucose sensing, among other uses.^[7] Finally, NIR light can be detected by inexpensive silicon-based detectors, making sensors based on these wavelengths cost-effective and easily deployed.^[8]

The biggest challenge inhibiting the further deployment of this technology today is the limited capability to efficiently generate broadband NIR light.^[9] Phosphor-converted NIR light-emitting diodes (pc-NIR LEDs) have been recently demonstrated to be the superior option for NIR production because of their outstanding output power, efficiency, durability, and compact size over other more traditional NIR light sources, including incandescent bulbs, tungsten halogen lamps, or even NIR LEDs.^[10,11] These advantages make pc-NIR LEDs ideal for accessible, low-cost spectroscopic applications. However, these devices require efficient and thermally stable phosphors to convert the nearly monochromatic blue emission from commercially available InGaN chips into the requisite broadband NIR light.

Generally, broadband NIR phosphors can be created by introducing an activator ion, like Eu²⁺, Bi²⁺, Mn²⁺, or Cr³⁺ into an inorganic solid-state host compound.^[12] Of the options available, Cr³⁺ in a weak crystal field environment, with its unique 3d³ electronic configuration, is considered the best option for broadband NIR emission.^[13,14] Cr³⁺ can be excited by blue light and emits between 700 and 1100 nm. This concept has led to the discovery of numerous Cr³⁺-substituted NIR phosphors. For example, garnets like Gd₃Sc₂Ga₃O₁₂:Cr³⁺ (full width at half maximum (fwhm) = 110 nm, $\lambda_{em} = 756$ nm) and Ca₃Sc₂Si₃O₁₂:Cr³⁺ (fwhm = 92 nm, $\lambda_{em} = 783$ nm) were both reported to have a quantum yield (QY) surpassing 90% and low thermal quenching, which is defined by the drop in emission

intensity at 150 °C (I_{150} °C). These properties indicate their potential for practical applications.^[15,16] Nevertheless, the emission peak of these materials is centered below 800 nm, and the fwhm is not sufficiently broad to cover the entire NIR region of interest (700–1100 nm). Other phosphors covering the entire NIR region have also been reported; however, their properties are less than satisfactory for practical application. These materials have either low QY values or poor thermal stability. For instance, $\text{LiInGe}_2\text{O}_6:\text{Cr}^{3+}$ (QY = 81%) has an I_{150} °C = 20%, indicating that more than 80% of the emission intensity is lost at high temperatures.^[17] $\text{LiInSi}_2\text{O}_6:\text{Cr}^{3+}$ (QY = 75%, I_{150} °C = 77%) and $\text{ScF}_3:\text{Cr}^{3+}$ (QY = 45%, I_{150} °C = 85.5%) have reasonable thermal stability, but relatively low efficiency.^[18,19] Therefore, it is vital to identify Cr^{3+} -activated phosphors that satisfy all three material requirements, including a high photoluminescence efficiency, thermally robust emission, and a broad spectrum emission covering the NIR region.

One of the primary research efforts currently being pursued to achieve materials worth creating prototype pc-NIR LED devices is by optimizing recently reported NIR phosphors through particle postprocessing. For example, the garnet phosphors $\text{Gd}_3\text{Sc}_2\text{Ga}_3\text{O}_{12}:\text{Cr}^{3+}$ and $\text{Ca}_3\text{Sc}_2\text{Si}_3\text{O}_{12}:\text{Cr}^{3+}$ were first reported to have a QY as low as 60% and 12.8%, respectively.^[20,21] Basore and co-workers improved their efficiency by substituting the larger Sc^{3+} with the smaller Al^{3+} cation.^[15] They relied on a Raman analysis to suggest that incorporating Al^{3+} inhibits the formation of antisite defects pushing the QY to near unity (99%). Similarly, Jia et al. showed the QY of $\text{Ca}_3\text{Sc}_2\text{Si}_3\text{O}_{12}:\text{Cr}^{3+}$ could be enhanced to 92% via synthesis process optimization, including preparing the sample under a reducing atmosphere to prevent the oxidation of Cr^{3+} to Cr^{4+} .^[16] They also identified the appropriate additives to obtain defect-free phosphors. These results convey an important message: the presence of defects, regardless of being internal antisite or external surface defects or the coexistence of Cr^{4+} in the product, will significantly reduce the luminescence efficiency of Cr^{3+} NIR phosphors. Therefore, when developing new Cr^{3+} phosphors, the first consideration for producing a highly efficient broadband NIR phosphor should involve minimizing the defect concentration and stabilizing chromium in its trivalent oxidation state.

Even if a nearly defect-free phosphor could be prepared, the large fwhm observed in Cr^{3+} materials stems from an enhanced electron–phonon coupling.^[22] However, significant electron–phonon coupling can also give rise to a significant loss in the photon emission intensity at elevated temperatures because of phonon-assisted nonradiative relaxation processes.^[23] Thus, it is essential to balance the fwhm, the material's efficiency, and temperature-dependent photoluminescence. One method that is useful for probing electron–phonon coupling is through the Huang–Rhys parameter (S).^[16,24] Generally, Cr^{3+} in oxide materials usually has a high S value, which means strong electron–phonon coupling and poor thermal stability. For example, $\text{Sr}_8\text{MgLa}(\text{PO}_4)_7:\text{Cr}^{3+}$ ($S = 7.9$, I_{150} °C \approx 10%), $\text{La}_3\text{Sc}_2\text{Ga}_3\text{O}_{12}:\text{Cr}^{3+}$ ($S = 6$, I_{150} °C \approx 58%), and $\text{CaSc}_2\text{O}_4:\text{Cr}^{3+}$ ($S = 5.3$, I_{150} °C \approx 20%) have a significant loss of photoluminescence at 150 °C.^[20,25,26] Conversely, fluorides have relatively weak electron–phonon coupling and are among the best materials developed thus far. For example, the $\text{K}_2\text{NaScF}_6:\text{Cr}^{3+}$ phosphor ($S = 2.96$) has an I_{150} °C = 89.6% and Lin et al. reported the $\text{ScF}_3:\text{Cr}^{3+}$ phosphor

($S = 3.01$) with an I_{150} °C = 85.5%.^[19,24] Unfortunately, many fluorides suffer from deliquescence, making them challenging to handle. Fluorine's high electronegativity may also cause issues stabilizing the Cr^{3+} oxidation state, leading to a drop in the quantum yield. Therefore, searching for a weak electron–phonon coupling oxide as a host matrix for Cr^{3+} is desirable.

In this work, GaTaO_4 was selected based on these considerations as a potentially ideal NIR phosphor. From the viewpoint of crystal chemistry, octahedral Ga^{3+} was expected to be occupied by Cr^{3+} , because Ga^{3+} ($r_{6\text{-coord.}} = 0.62$ Å) has the same valence state and nearly identical ionic radius compared to Cr^{3+} ($r_{6\text{-coord.}} = 0.615$ Å).^[27] This size and charge match is beneficial for reducing the probability of defects and minimize any possible local crystal structure distortions caused by substitution. The heavy atom (Ta) is also expected to minimize electron–phonon coupling.^[28] Furthermore, the structural rigidity and electronic structure were evaluated by quantum chemical calculation, confirming appropriate rigidity, sufficient bandgap, and a suitable electronic environment for maintaining Cr^{3+} . The subsequent synthesis of the $\text{GaTaO}_4:\text{Cr}^{3+}$ phosphor demonstrates a highly efficient long-wavelength broadband NIR emission ($\lambda_{\text{em}} = 840$ nm, fwhm = 140 nm) with the QY as high as 91% under 460 nm excitation, placing it among the best reported long-wavelength broadband NIR phosphors. The emission intensity maintains 85% of the room temperature intensity at 100 °C, which is generally the working temperature of NIR-LEDs,^[24] indicating that an excellent thermal stability is achieved. The fabricated pc-LED device has an intense NIR light emission (178 mW at 500 mA) with photoelectric efficiency of 6%, demonstrating the great potential of this material for next-generation pc-NIR-LED applications.

2. Results and Discussion

2.1. Phase, Crystal Structure, and Morphology

The phase purity of the Cr^{3+} -substituted analogs with the general substitution scheme $\text{Ga}_{1-x}\text{Cr}_x\text{TaO}_4$ ($x = 0\text{--}0.02$) was first checked by laboratory powder X-ray diffraction (Figure S1, Supporting Information). All the diffraction peaks can be indexed to GaTaO_4 standard phase in the inorganic crystal structure database (ICSD no. 32702),^[29] demonstrating the successful synthesis of the target product with high purity. To further determine the crystal structure, a Rietveld refinement of the synchrotron X-ray powder diffraction data for the undoped GaTaO_4 sample was performed with the results plotted in Figure 1a. The refinement statistics are provided in Table 1 and the refined atomic coordinates are provided in Table S1 in the Supporting Information. These data indicate the product's excellent phase purity and confirm the crystal structure. GaTaO_4 adopts a monoclinic crystal structure with the space group of $P2_1/c$ (no. 13). The crystal structure contains two crystallographic independent octahedral environments, GaO_6 and TaO_6 . These units form edge-sharing connections between the same type of octahedra, while corner-sharing occurs between different octahedral units. Viewing a $2 \times 2 \times 2$ supercell of the GaTaO_4 crystal structure, illustrated in Figure 1b, shows that the compound can be divided into GaO_6 layers and TaO_6 layers

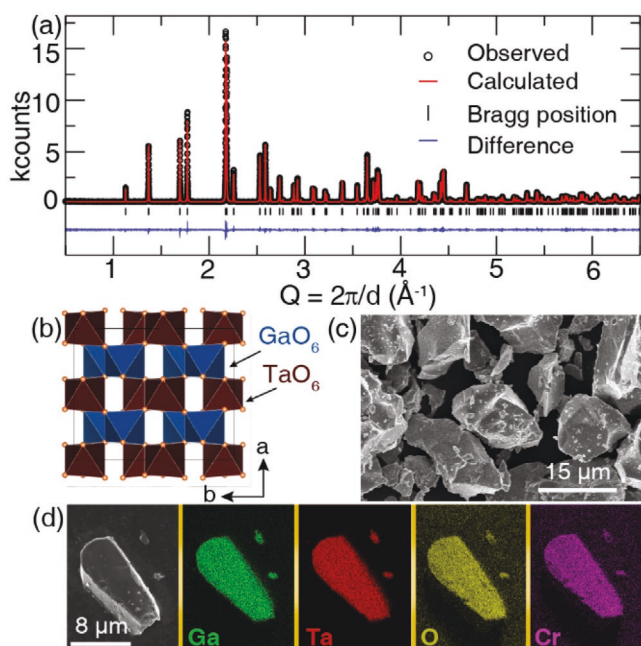


Figure 1. a) Rietveld refinement of the synchrotron X-ray powder diffraction data for GaTaO₄ sample, b) crystal structure of GaTaO₄ with 2 × 2 × 2 supercell, c) scanning electron microscopy (SEM), and d) energy-dispersive X-ray (EDS) mapping of Ga_{0.994}Cr_{0.006}TaO₄.

that form a wall-like structure. The substitution of Cr³⁺ into the crystal structure is expected to occur on the Ga³⁺ crystallographic position based on the similar ionic radius of these two ions (Cr³⁺ $r_{6\text{-coord.}}$ = 0.615 Å; Ga³⁺ $r_{6\text{-coord.}}$ = 0.62 Å; and Ta⁵⁺ $r_{6\text{-coord.}}$ = 0.64 Å) and the ion's isovalency.^[27] However, it is also necessary to bear in mind the possibility of Cr³⁺ substituting for the Ta⁵⁺ site based on their similar ionic radii.

Analyzing the morphology of selected Ga_{0.994}Cr_{0.006}TaO₄ particles using scanning electron microscopy (SEM), presented in Figure 1c, reveals the sample out of the furnace has an irregular morphology with the average particle size falling in the range of 5 to 15 μm. Mapping the elemental distribution on a randomly selected particle (Figure 1d) using energy-dispersive X-ray

Table 1. The refined crystal structure data.

Formula	GaTaO ₄
Radiation type; λ [Å]	Synchrotron; 0.4581530
Q range [Å ⁻¹]	0.5–6.5
Temperature [°C]	25
Space group; Z	P2 ₁ /c; 2
a [Å]	4.5929(5)
b [Å]	5.5690(9)
c [Å]	4.9651(6)
β [°]	89.60(8)
Unit cell volume [Å ³]	126.99(8)
Profile R-factor, R _p	0.0704
Weighted profile R-factor, R _{wp}	0.0914
χ ²	1.468

spectrometry (EDS) demonstrated that only the loaded elements (Ga, Ta, Cr, and O) are detected in the product, and all of the elements are uniformly distributed throughout the particle.

2.2. Site Occupation, Electronic Properties, and Structural Rigidity

Considering the crystal structure of GaTaO₄ contains two crystallographically independent octahedral sites that could be occupied by the Cr³⁺ ion, it is necessary to determine the site preference of Cr³⁺. The low substitution concentration of Cr³⁺ in the compound (<2 mol%) makes experimentally identifying the site preference challenging. However, first-principles calculations have proven reliable to establish the most likely location of the metal substitution site based on the relative formation energies.^[30] Here, we calculate the compound Ga_{0.9375}Cr_{0.0625}TaO₄ with three substitution patterns. One model is Cr_{Ga}, where Cr³⁺ can directly occupy the Ga³⁺ site. The second model is Cr_{Ta}^{''}+Ta_{Ga}^{''}, where Cr³⁺ is set to occupy the Ta⁵⁺ site and to maintain charge balance, an additional Ta⁵⁺ is placed on a Ga³⁺ site. The third model is the most complex, Cr_{Ga}+Ta_{Ga}^{''}+Ga_{Ta}^{''}, where Cr³⁺ is placed on the Ga³⁺ site while an additional Ta⁵⁺-Ga³⁺ antisite (neutral) defect is created. Calculating the relative substitution/defect formation energies using the hybrid-level of theory, provided in Table S2 in the Supporting Information, reveals that Cr³⁺ directly substituting the Ga³⁺ site has a dramatic energy preference of nearly 1 eV per atom. This result indicates that Cr³⁺ not only has a strong energetic preference to occupy the Ga³⁺ site rather than the Ta⁵⁺ site but, more importantly, that substituting Cr³⁺ for Ga³⁺ is not predicted to generate any antisite defects in this material, which would have reduced the QY of the sample.

Further understanding the deformation of the charge density in GaTaO₄ due to the substitution of Cr³⁺ was investigated to establish the potential for stabilizing the preferred trivalent state of chromium over its other potential oxidation states. As depicted in Figure S2 in the Supporting Information, the O²⁻ anions surrounding Cr³⁺ can attract electrons from the substituted cation, as expected based on electronegativity differences. Notably, the Ta⁵⁺ ion also transfers a significant charge density to the same O²⁻ anions. Following the inductive effect, the next-nearest tantalum neighbor injects electrons into the oxygen anions, making it easier to stabilize the 3+ valence state of Cr. Finally, the density of states of Ga_{0.9375}Cr_{0.0625}TaO₄ was calculated using the HSE06 hybrid functional and compared with undoped GaTaO₄, as shown in Figure 2. The bandgap of GaTaO₄ was calculated to be 4.82 eV. The top of the valence band of both compounds was determined by O 2p states, whereas the Ta 5d states dominate the bottom of the conduction band. The Cr 3d states are present in the bandgap and split into occupied t_{2g} and unoccupied e_g states. The substitution of Cr caused a slight shift of the conduction band toward low energy.

Given that GaTaO₄ has a reasonably low likelihood of significant defect formation and an electronic structure conducive to stabilizing the desired Cr³⁺ cation, it is worth determining the structural rigidity of the phase, which is a proxy for the QY. Structural rigidity is considered highly related to the QY because the high rigidity of the host material inhibits soft

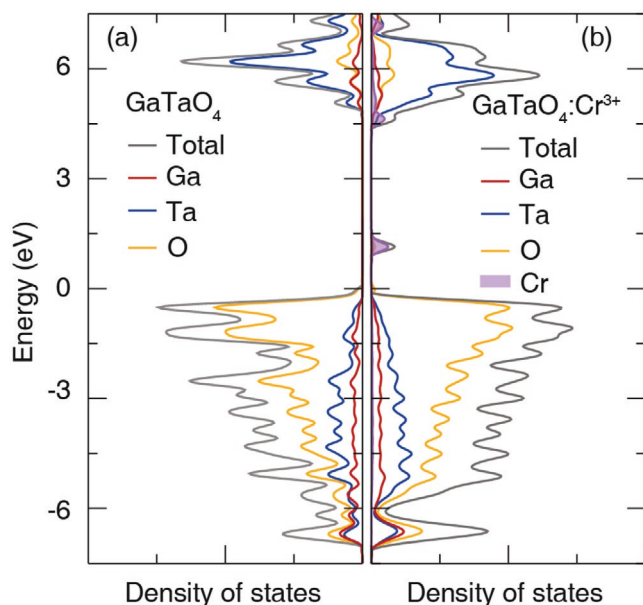


Figure 2. Calculated density of states of a) GaTaO₄ and b) Ga_{0.9375}Cr_{0.0625}TaO₄ using the HSE06 hybrid functional.

phonon modes that lead to nonradiative relaxation, thereby increasing the propensity for photon emission.^[31] Work has suggested that a material's Debye temperature (Θ_D) is a reliable single numerical proxy for structural rigidity in rare-earth substituted phosphors.^[32] Therefore, it is also tested here to see the extent of applying Θ_D to predict Cr³⁺ material's photoluminescence efficiency. GaTaO₄, along with a few other reported broadband NIR phosphors, were evaluated via density functional theory (DFT) calculations.^[18,19,33,34] The calculated Θ_D along with experimental QY are provided in Table S3 in the Supporting Information. GaTaO₄ has a higher Θ_D value (567 K) than most of the listed compounds, such as LiInSi₂O₆ (550 K), Ga₂O₃ (530 K), ScF₃ (534 K), BaMgAl₁₀O₁₇ (513 K).^[35] Thus, it is likely that a high QY can be expected when substituting Cr³⁺ in the title host crystal structure.

2.3. Photoluminescence

The diffuse reflectance (DR) spectra of GaTaO₄ and Ga_{0.994}Cr_{0.006}TaO₄ were collected and plotted in Figure 3a. The Cr³⁺-substituted samples exhibit intense absorption in the blue and red regions of the visible spectrum, corresponding to the ⁴A₂ → ⁴T₁ and ⁴A₂ → ⁴T₂ Cr³⁺ electronic transitions, respectively. The optical bandgap (E_g) of GaTaO₄ can be evaluated by fitting the data with Equation (1)^[36,37]

$$[hv\alpha]^{\frac{1}{n}} = A(hv - E_g) \quad (1)$$

where hv , α , E_g , and A refer to the photon energy, absorption coefficient, bandgap, and proportionality constant, respectively. The value of the exponent n is determined by the nature of the electronic transition. For direct allowed transition, direct forbidden transition, indirect allowed transition, and indirect forbidden transition, n is 1/2, 3/2, 2, and 3, respectively. The

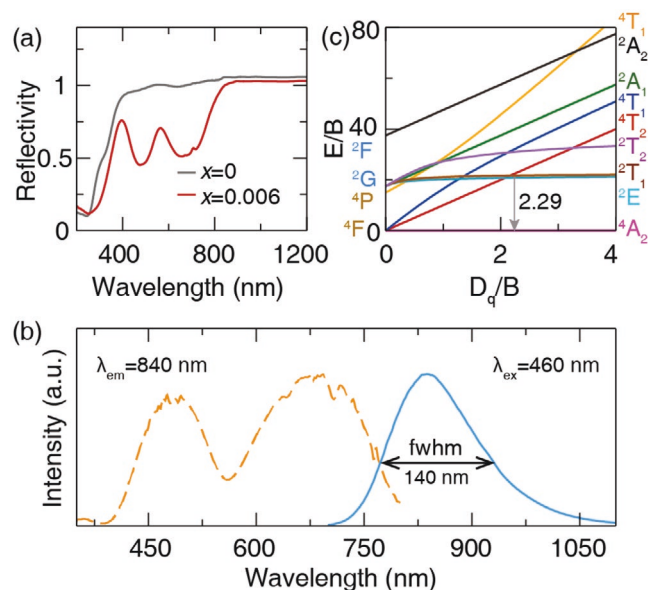


Figure 3. a) Diffuse reflectance spectra of GaTaO₄ and Ga_{0.994}Cr_{0.006}TaO₄, b) photoluminescence excitation spectrum of Ga_{0.994}Cr_{0.006}TaO₄, and c) Tanabe–Sugano diagram for Cr³⁺ in an octahedral site.

electronic band structure (Figure S3, Supporting Information) of GaTaO₄ indicates an indirect bandgap with an allowed transition ($n = 2$), which results in an optical bandgap of 4.61 eV (Figure S4, Supporting Information). This is in good agreement with the computationally obtained bandgap of 4.82 eV. This experimental E_g value is much larger than LiInSi₂O₆ (3.45 eV),^[18] but slightly lower than Ga₂O₃ (4.78 eV).^[38]

The room temperature photoluminescence excitation and emission spectra of Ga_{0.994}Cr_{0.006}TaO₄ were then collected. As shown in Figure 3b, the excitation spectrum covers a wide region spanning from 400 to 800 nm. There are excitation peaks centered at 485 and 692 nm corresponding to the ⁴A₂ → ⁴T₁ and ⁴A₂ → ⁴T₂ spin-allowed transitions of Cr³⁺ in a weak octahedral crystal field.^[39,40] The crystal field strength can be characterized by crystal field splitting (Dq) and the Racah parameter (B) calculated using Equations (2)–(4)^[41]

$$10Dq = E(^4T_2) - E(^4A_2 \rightarrow ^4T_2) \quad (2)$$

$$\frac{Dq}{B} = \frac{15(x-8)}{x^2-10x} \quad (3)$$

$$x = \frac{E(^4A_2 \rightarrow ^4T_1) - E(^4A_2 \rightarrow ^4T_2)}{Dq} \quad (4)$$

Examining the data reveals calculated Dq and B parameters of 1445.0 and 631.5 cm⁻¹, resulting in a $Dq/B = 2.29$ (Figure 3c). This suggests that the compound provides a relatively weak crystal field for Cr³⁺.

The emission spectrum of the sample contains a broad emission covering the 700–1100 nm region with the peak centered at 840 nm and a fwhm of 140 nm, corresponding to the ⁴T₂ → ⁴A₂ transition of Cr³⁺. Decomposing the emission spectrum shows that a single Gaussian function cannot fit the data,

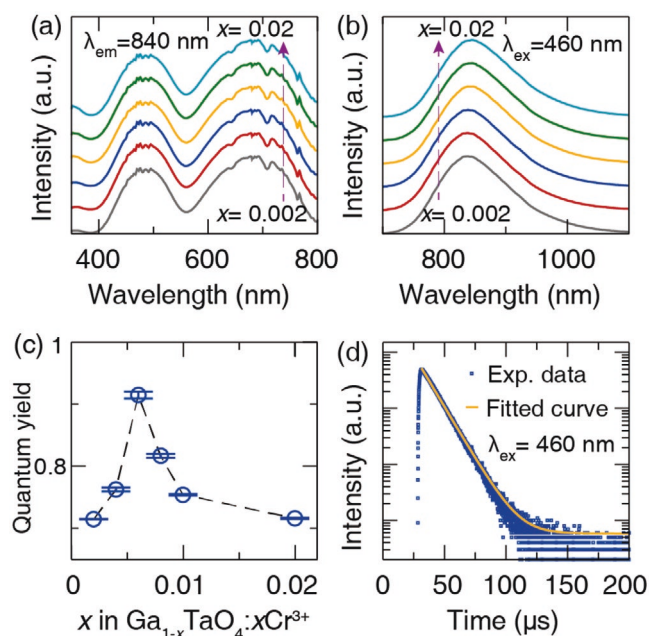


Figure 4. a) Room temperature excitation spectra ($\lambda_{em} = 840$ nm) and b) emission spectra ($\lambda_{ex} = 460$ nm) of $Ga_{1-x}Cr_xTaO_4$ ($x = 0.002, 0.004, 0.006, 0.008, 0.01,$ and 0.02) phosphor; c) quantum yield as a function of Cr^{3+} concentration; and d) decay curve of $Ga_{0.994}Cr_{0.006}TaO_4$ excited by 460 nm, monitored at 840 nm, and fitted by single exponential function.

but instead requires two Gaussian functions centered at 881, and 824 nm, respectively (Figure S5, Supporting Information). This usually indicates two distinct emission centers existing in this phosphor. However, the normalized emission spectrum when excited at different wavelengths ($\lambda_{ex} = 285, 480, 580,$ and 680 nm) and the normalized excitation spectrum monitored at different wavelengths ($\lambda_{em} = 770, 840, 900,$ and 1000 nm) (Figure S6, Supporting Information) are nearly overlapped, demonstrating that there are not two crystallographically independent emission sites. Instead, the asymmetric emission spectrum may arise from a local structure distortion around the Cr^{3+} cation, which induces inhomogeneous peak broadening.^[42] The distortion causes low site symmetry, supporting by the splitting of vibrational peaks as indicated in Raman spectra (Figure S7, Supporting Information).

Further, varying the Cr^{3+} concentration from 0.2% to 2% indicates that the excitation spectra (Figure 4a) are nearly unchanged while the emission spectra (Figure 4b) present a slight redshift (≈ 8 nm). The constant position of the excitation spectrum indicates the crystal field splitting is not significantly perturbed with varying Cr^{3+} concentration, mainly due to the rigidity of crystal structure and low substitution concentration. A very slight redshift of the emission spectra is observed with increasing Cr^{3+} , but this is only a minor change suggesting the local environment is nearly constant. The optimized Cr^{3+} concentration is 0.6% (Figure 4c), beyond which concentration quenching becomes significant. Under 460 nm excitation, the QY of $Ga_{0.994}Cr_{0.006}TaO_4$ is determined to be 91.2% (Figure S8, Supporting Information), which easily surpasses the best reported phosphor, $LiInGe_2O_6:Cr^{3+}$ (QY = 81%),^[17] in long-wavelength NIR region ($\lambda_{em} > 830$ nm). The absorptivity

of $Ga_{0.994}Cr_{0.006}TaO_4$ is determined to be 34.3%, which is higher than $Gd_3Sc_2Ga_3O_{12}:Cr^{3+}$ ($\approx 20\%$) and $Ga_2O_3:Cr^{3+}$ (30.7%),^[15,23] supporting the impressive 31.3% external quantum efficiency of this phosphor. These results demonstrate that $GaTaO_4:Cr^{3+}$ is a highly efficient long-wavelength broadband NIR phosphor under 460 nm blue light excitation.

The room temperature photoluminescence decay curve of $Ga_{0.994}Cr_{0.006}TaO_4$ was collected by exciting the phosphor at 460 nm and monitoring at 840 nm, as shown in Figure 4d. The decay curve can be fit by a single exponential function with a lifetime of 11.8 μs . These results also support that only one type of emission center (Cr_{Ga}) dominates the luminescence in this phosphor, in agreement with the steady-state photoluminescence data. Nevertheless, a small amount of $Cr_{Ta}''+Ta_{Ga}''$ may also inevitably generate from the high-temperature (1450 $^{\circ}C$) synthetic procedures used to make the product, although there is no strong spectroscopic evidence for this alternative Cr^{3+} substitution. With the increase of Cr^{3+} concentration from 0.2% to 2%, the decay curves (Figure S9, Supporting Information) present a minor decrease in the lifetime (11.9–11.0 μs), which is caused by the concentration quenching effect.

The thermal stability of $Ga_{0.994}Cr_{0.006}TaO_4$ was analyzed by collecting the temperature-dependent emission spectra from 298 to 473 K, under 460 nm excitation. The raw spectra are provided in Figure S10a in the Supporting Information. The contour plot of the spectra and normalized integrated (peak) intensity as a function of temperature are plotted in Figure 5a,b, respectively. The emission intensity gradually decreases with increasing temperature. When heated to 373 and 423 K, the integrated emission intensity of $Ga_{0.994}Cr_{0.006}TaO_4$ remains about 85% and 60%, respectively, of the room temperature (298 K) value. A relatively narrow energy gap between the conduction band and e_g states of Cr^{3+} was observed in the electronic structure of $Ga_{0.9375}Cr_{0.0625}TaO_4$ as shown in Figure 2, which likely causes the thermal ionization at high temperatures, leading to the decrease of emission intensity in the temperature region from 398 to 473 K. Nevertheless, compared to other reported long-wavelength broadband NIR oxide phosphors, listed in Table 2, $Ga_{0.994}Cr_{0.006}TaO_4$ offers competitive thermal stability up to 373 K, and superior thermal stability by 423 K. Moreover, increasing the temperature indicates the emission peak position and band width of the emission spectra changed as well (Figure S10b, Supporting Information). The peak position's redshift stems from a temperature-induced weakening of the crystal field environment, while the broadening of emission peak is due to the increasing amount of electrons excited at higher vibration levels with the increase of temperature.^[23,24]

For Cr^{3+} -activated phosphor materials, the thermal stability is highly related to the strength of phonon–electron coupling, which can be characterized by Huang–Rhys factor (S) obtained by fitting Equation (5)^[43,44]

$$fwhm(T) = \sqrt{8 \ln 2} \times \hbar\omega \times \sqrt{\coth(\hbar\omega/2kT)} \quad (5)$$

where the fwhm (eV) is the full width at half maximum of emission spectrum at temperature T (K), and the $\hbar\omega$ and k are the phonon energy and Boltzmann's constant, respectively. Fitting the data using this equation results in Figure 5c. The resulting S and $\hbar\omega$ are calculated to be 3.82 and 64.43 meV,

Table 2. Quantum yield and thermal stability of Cr³⁺-doped long-wavelength broadband NIR phosphors, and photoelectric performance of fabricated pc-LED devices.

Phosphor	λ_{em} [nm]	QY [%]	$I_{100\text{ }^\circ\text{C}}$ and $I_{150\text{ }^\circ\text{C}}$ [%]	NIR output power [mW]@photoelectric efficiency	Ref.
GaTaO ₄ :Cr ³⁺	840	91	85, 60	178@6%	This work
LiScP ₂ O ₇ :Cr ³⁺	880	53	42, =18	19@7%	[51]
LiInSi ₂ O ₆ :Cr ³⁺	840	75	=88, 77	52@17%	[18]
LiInGe ₂ O ₆ :Cr ³⁺	880	81	45, =20	–	[17]
LiIn ₂ SbO ₆ :Cr ³⁺	970	7	=10, –	–	[6]
LaSc ₃ B ₄ O ₁₂ :Cr ³⁺	871	23	58, 30	–	[14]
(La,Y)Sc ₃ B ₄ O ₁₂ :Cr ³⁺	850	41	41, =20	11@4%	[52]
BaZrGe ₃ O ₉ :Cr ³⁺	830	–	70, 53	3@1%	[53]
ScF ₃ :Cr ³⁺	853	45	–, 86	8@3%	[19]

respectively. These values show only a slight deviation from the empirical equation $S = (1/2 E_{\text{Stokes}}/\hbar\omega + 1/4) \pm 1/4$ (Figure S11, Supporting Information), validating this result. The Huang–Rhys S value is clearly lower than most reported broadband NIR oxide phosphors as listed in Table S4 in the Supporting Information, demonstrating that a relatively weak electron–phonon coupling exists in this material, as desired.

2.4. Application to NIR pc-LEDs

Finally, the practical application of GaTaO₄:Cr³⁺ phosphor was evaluated. A prototype pc-NIR-LED device (shown in the inset of Figure 6a) was fabricated by combining the as-prepared

Ga_{0.994}Cr_{0.006}TaO₄ phosphor with a 460 nm blue InGaN chip. As presented, the body color of this phosphor is gray-green, indicating the strong absorption of the powder in the visible region. The electroluminescence (EL) spectra of the NIR-LED device at different forward bias currents (50–1000 mA) are presented in Figure 6a, while the NIR output power and NIR photoelectric efficiency as a function of current are demonstrated in Figure 6b and Table S5 in the Supporting Information. As shown, the output power gradually increases from 20.2 to 259 mW, indicating the GaTaO₄:Cr³⁺ phosphor has potential in high-power NIR LED devices. The photoelectric conversion efficiency gradually decreases from 8.2% to 4% but would be even better if the data above 1000 nm were included in the calculation. It is noted that the NIR output power reaches 178 mW,

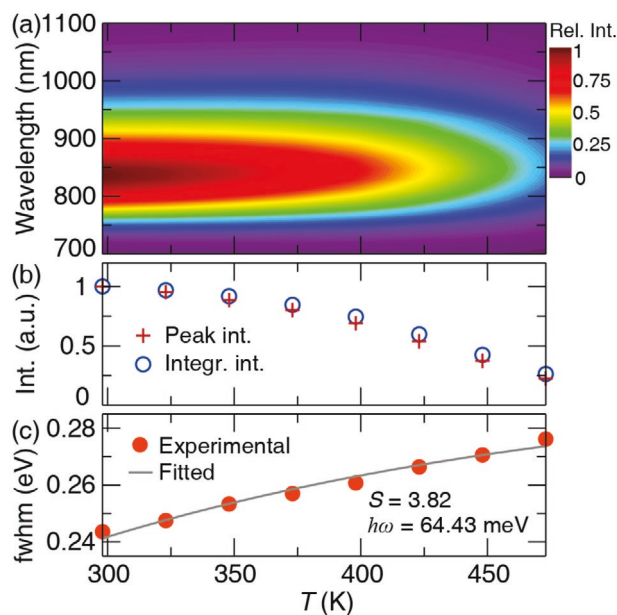


Figure 5. a) Contour plot of the emission spectra of Ga_{0.994}Cr_{0.006}TaO₄ phosphor excited at 460 nm as a function of temperature, b) normalized integrated intensity of the emission spectra (norm. integr. int.) and normalized intensity of the emission peak (norm. peak int.) as a function of temperature, and c) theoretically fitting the experimental fwhm of the emission spectra of Ga_{0.994}Cr_{0.006}TaO₄ phosphor as a function of temperature.

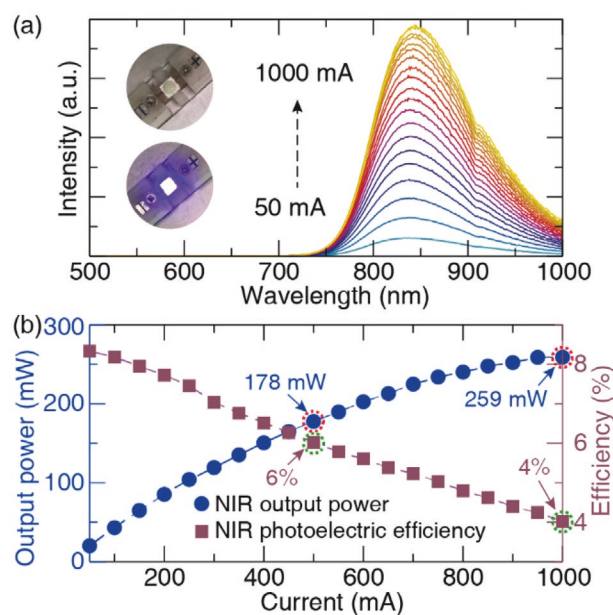


Figure 6. a) Photoluminescence spectra of the fabricated pc-NIR-LED device that combines a 460 nm InGaN blue LED chip with Ga_{0.994}Cr_{0.006}TaO₄ NIR phosphor under a forward bias of 50–1000 mA. The insets show the photographs of the LED device. b) Output power and photoelectric conversion efficiency of NIR device as a function of driven current in the range of 50 to 1000 mA.

and photoelectric efficiency of 6%, under the drive current of 500 mA, implying a better performance than the well-known $\text{Ca}_3\text{Sc}_2\text{Si}_3\text{O}_{12}:\text{Cr}^{3+}$ phosphor (109.9 mW@ 3.8%, under a drive current of 520 mA).^[16] While comparing with Cr^{3+} -doped long-wavelength ($\lambda_{\text{em}} > 830$ nm) broadband NIR phosphors (listed in Table 2), it shows the impressive performance of the $\text{GaTaO}_4:\text{Cr}^{3+}$ phosphor for the next-generation broadband pc-NIR-LEDs.

3. Conclusions

In summary, a highly efficient and thermally stable broadband emitting $\text{GaTaO}_4:\text{Cr}^{3+}$ NIR phosphor has been identified. The site occupancy of Cr^{3+} was verified to be on the Ga^{3+} site. This phosphor can be efficiently excited by 460 nm blue light to produce a broadband long-wavelength emission ($\lambda_{\text{em}} = 840$ nm, fwhm = 140 nm) with a high QY of 91%. The emission intensity at 373 K remains 85% of that at room temperature, demonstrating high thermal stability of this material due to the relatively weak phonon–electron coupling with Huang–Rhys S value as low as 3.82. Finally, the performance of a prototype pc-NIR-LED device fabricated by using the as-prepared phosphor was evaluated. Under a driving current of 500 mA, the NIR output power and photoelectric conversion efficiency of this device were determined to be 178 mW and 6%, respectively, indicating this phosphor has great potentials for pc-NIR-LED applications.

4. Experimental Section

Synthesis: Samples with the general formula $\text{Ga}_{1-x}\text{Cr}_x\text{TaO}_4$ ($x = 0, 0.002, 0.004, 0.006, 0.008, 0.01, \text{ and } 0.02$) were prepared using a high-temperature, solid-state chemical route with Ga_2O_3 (Aldrich, 99.95%), Ta_2O_5 (Aldrich, 99.9%), and Cr_2O_3 (Aldrich, 99.99%) employed as the starting materials. The powders were weighed out according to the required stoichiometric ratio and ground using an agate mortar and pestle. The homogeneous mixtures were then placed in an alumina crucible and heated to 1450 °C with a heating rate of 3 °C min^{-1} and held for 8 h in air followed by cooling at 3 °C min^{-1} . The final products were ground into a fine powder using an agate mortar and pestle.

Characterization: The X-ray diffractograms (X'Pert3 PANalytical; Cu K_{α} , $\lambda = 1.5406$ Å) were collected to confirm phase purity for each nominally loaded composition. Synchrotron X-ray powder diffraction data were collected at 298 K using beamline 11-BM at the Advanced Photon Source with a calibrated wavelength of 0.4581530 Å. The Rietveld refinement was performed with the General Structure Analysis System software and the EXPGUI interface to determine the exact crystal structure.^[45] SEM was used to image the particles, while energy-dispersive X-ray spectroscopy (EDS) elemental maps were collected to confirm the elemental composition. These data were collected on a Hitachi-S4800 (Japan).

The room temperature photoluminescence, temperature-dependent photoluminescence, and time-gated photoluminescence decay curves of the Cr^{3+} -substituted compounds were collected using an FLS-980 fluorescence spectrophotometer (Edinburgh Instruments) equipped with a Xenon flash lamp (450 W, Osram) excitation source. The quantum yields were measured using a Quantaurus-QY Plus C13534-11 (Hamamatsu Photonics). The DR spectra were detected on a UV–vis–NIR spectrophotometer (SHIMADZU, Japan) with an integrated sphere attachment and BaSO_4 powder as a standard.

The NIR LED device was fabricated by coating a mixture of the as-prepared $\text{Ga}_{0.994}\text{Cr}_{0.006}\text{TaO}_4$ phosphor and resin with a 1:1 ratio in

weight on a high-power 460 nm blue LED. The electroluminescence spectrum, output power, and photoelectric conversion efficiency of the fabricated NIR pc-LED device were measured using an HAAS2000 photoelectric measuring system (EVERFINE, China).

Computation: The crystal structures of GaTaO_4 and $\text{Ga}_{0.9375}\text{Cr}_{0.0625}\text{TaO}_4$, were optimized using the Vienna ab initio Simulation Package, which is a plane-wave pseudopotential total energy package based on density functional theory (DFT).^[46] The atomic positions and lattice parameters were relaxed with electronic convergence criteria of 1×10^{-5} eV and atomic convergence criteria 0.01 eV Å⁻¹. The cutoff energy of 500 eV was used for the basis set of the plane waves, and a $4 \times 4 \times 4$ Γ -centered Monkhorst–Pack k -point grid was used to sample the first Brillouin zone. The Perdew–Burke–Ernzerhof (PBE) exchange–correlation functional was employed for structure optimization, formation energy, and charge density calculations,^[47–49] whereas the subsequent electronic properties were determined using the HSE06 hybrid functional.^[50]

Supporting Information

Supporting Information is available from the Wiley Online Library or from the author.

Acknowledgements

The authors thank the National Natural Science Foundation of China (no. 51702057) and the National Science Foundation (DMR-1847701). This research used the Maxwell/Opuntia/Sabine cluster(s) operated by the University of Houston and the Research Computing Data Core (RCDC).

Conflict of Interest

The authors declare no conflict of interest.

Data Availability Statement

Research data are not shared.

Keywords

DFT calculations, light-emitting diodes, luminescence, materials design, near-infrared emission, oxides

Received: August 26, 2021

Revised: September 24, 2021

Published online:

- [1] M. Manley, *Chem. Soc. Rev.* **2014**, *43*, 8200.
- [2] L. S. Magwaza, U. L. Opara, H. Nieuwoudt, P. J. R. Cronje, W. Saeys, B. Nicolai, *Food Bioprocess Technol.* **2012**, *5*, 425.
- [3] F. Scholkmann, S. Kleiser, A. J. Metz, R. Zimmermann, J. Mata Pavia, U. Wolf, M. Wolf, *Neuroimage* **2014**, *85*, 6.
- [4] B. Grassi, V. Quaresima, *J. Biomed. Opt.* **2016**, *21*, 091313.
- [5] R. J. Xie, *Light: Sci. Appl.* **2020**, *9*, 9.
- [6] G. Liu, T. Hu, M. S. Molokeev, Z. Xia, *iScience* **2021**, *24*, 102250.
- [7] A. A. Lucero, G. Addae, W. Lawrence, B. Neway, D. P. Credeur, J. Faulkner, D. Rowlands, L. Stoner, *Exp. Physiol.* **2018**, *103*, 90.
- [8] H. Zeng, T. Zhou, L. Wang, R. J. Xie, *Chem. Mater.* **2019**, *31*, 5245.

- [9] G. N. A. D. Guzman, V. Rajendran, Z. Bao, M. H. Fang, W. K. Pang, S. Mahlik, T. Lesniewski, M. Grinberg, M. S. Molokeev, G. Leniec, S. M. Kaczmarek, J. Ueda, K. M. Lu, S. F. Hu, H. Chang, R. S. Liu, *Inorg. Chem.* **2020**, *59*, 15101.
- [10] V. Rajendran, M.-H. Fang, G. N. De Guzman, T. Lesniewski, S. Mahlik, M. Grinberg, G. Leniec, S. M. Kaczmarek, Y.-S. Lin, K.-M. Lu, C.-M. Lin, H. Chang, S.-F. Hu, R.-S. Liu, *ACS Energy Lett.* **2018**, *3*, 2679.
- [11] M.-H. Fang, P.-Y. Huang, Z. Bao, N. Majewska, T. Lesniewski, S. Mahlik, M. Grinberg, G. Leniec, S. M. Kaczmarek, C.-W. Yang, K.-M. Lu, H.-S. Sheu, R.-S. Liu, *Chem. Mater.* **2020**, *32*, 2166.
- [12] Y. Wei, P. Dang, Z. Dai, G. Li, J. Lin, *Chem. Mater.* **2021**, *33*, 5496.
- [13] G. N. A. De Guzman, M.-H. Fang, C.-H. Liang, Z. Bao, S.-F. Hu, R.-S. Liu, *J. Lumin.* **2020**, *219*, 116944.
- [14] T. Gao, W. Zhuang, R. Liu, Y. Liu, C. Yan, X. Chen, *Cryst. Growth Des.* **2020**, *20*, 3851.
- [15] E. T. Basore, W. Xiao, X. Liu, J. Wu, J. Qiu, *Adv. Opt. Mater.* **2020**, *8*, 2000296.
- [16] Z. Jia, C. Yuan, Y. Liu, X.-J. Wang, P. Sun, L. Wang, H. Jiang, J. Jiang, *Light: Sci. Appl.* **2020**, *9*, 86.
- [17] T. Liu, H. Cai, N. Mao, Z. Song, Q. Liu, *J. Am. Ceram. Soc.* **2021**, *104*, 4577.
- [18] X. Xu, Q. Shao, L. Yao, Y. Dong, J. Jiang, *Chem. Eng. J.* **2020**, *383*, 123108.
- [19] Q. Lin, Q. Wang, M. Liao, M. Xiong, X. Feng, X. Zhang, H. Dong, D. Zhu, F. Wu, Z. Mu, *ACS Appl. Mater. Interfaces* **2021**, *13*, 18274.
- [20] B. Malysa, A. Meijerink, T. Jüstel, *J. Lumin.* **2018**, *202*, 523.
- [21] L. Yao, Q. Shao, X. Xu, Y. Dong, C. Liang, J. He, J. Jiang, *Ceram. Int.* **2019**, *45*, 14249.
- [22] M.-H. Fang, K.-C. Chen, N. Majewska, T. Lesniewski, S. Mahlik, G. Leniec, S. M. Kaczmarek, C.-W. Yang, K.-M. Lu, H.-S. Sheu, R.-S. Liu, *ACS Energy Lett.* **2021**, *6*, 109.
- [23] J. Zhong, Y. Zhuo, F. Du, H. Zhang, W. Zhao, J. Brgoch, *ACS Appl. Mater. Interfaces* **2021**, *13*, 31835.
- [24] E. Song, H. Ming, Y. Zhou, F. He, J. Wu, Z. Xia, Q. Zhang, *Laser Photonics Rev.* **2021**, *15*, 2000410.
- [25] B. Malysa, A. Meijerink, T. Jüstel, *Opt. Mater. (Amsterdam, Neth.)* **2018**, *85*, 341.
- [26] B. Malysa, A. Meijerink, W. Wu, T. Jüstel, *J. Lumin.* **2017**, *190*, 234.
- [27] R. D. Shannon, *Acta Crystallogr., Sect. A: Found. Crystallogr.* **1976**, *32*, 751.
- [28] S. Ye, Q. Liu, C. Chen, J. Lin, X. Yue, J. Ding, Q. Wu, *ACS Sustainable Chem. Eng.* **2021**, *9*, 8848.
- [29] L. Perfler, V. Kahlenberg, D. Töbrens, A. Schaur, M. Tribus, M. Orlova, R. Kaindl, *Inorg. Chem.* **2016**, *55*, 5384.
- [30] J. Zhong, Y. Zhuo, S. Hariyani, W. Zhao, J. Wen, J. Brgoch, *Chem. Mater.* **2020**, *32*, 882.
- [31] J. Brgoch, S. P. DenBaars, R. Seshadri, *J. Phys. Chem. C* **2013**, *117*, 17955.
- [32] Y. Zhuo, A. Mansouri Tehrani, A. O. Oliynyk, A. C. Duke, J. Brgoch, *Nat. Commun.* **2018**, *9*, 4377.
- [33] M. H. Fang, G. N. A. De Guzman, Z. Bao, N. Majewska, S. Mahlik, M. Grinberg, G. Leniec, S. M. Kaczmarek, C. W. Yang, K. M. Lu, H. S. Sheu, S. F. Hu, R. S. Liu, *J. Mater. Chem. C* **2020**, *8*, 11013.
- [34] L. You, R. Tian, T. Zhou, R. Xie, *Chem. Eng. J.* **2021**, *417*, 129224.
- [35] S. Hariyani, A. C. Duke, T. Krauskopf, W. G. Zeier, J. Brgoch, *Appl. Phys. Lett.* **2020**, *116*, 051901.
- [36] P. Makuła, M. Pacia, W. Macyk, *J. Phys. Chem. Lett.* **2018**, *9*, 6814.
- [37] J. Tauc, R. Grigorovici, A. Vancu, *Phys. Status Solidi* **1966**, *15*, 627.
- [38] N. Makeswaran, A. K. Battu, R. Swadipita, F. S. Mancini, C. V. Ramana, *ECS J. Solid State Sci. Technol.* **2019**, *8*, Q3249.
- [39] B. Bai, P. Dang, D. Huang, H. Lian, J. Lin, *Inorg. Chem.* **2020**, *59*, 13481.
- [40] G. Liu, M. S. Molokeev, B. Lei, Z. Xia, *J. Mater. Chem. C* **2020**, *8*, 9322.
- [41] B. Struve, G. Huber, *Appl. Phys. B: Photophys. Laser Chem.* **1985**, *36*, 195.
- [42] S. A. Payne, L. L. Chase, G. D. Wilke, *J. Lumin.* **1989**, *44*, 167.
- [43] F. Zhao, Z. Song, J. Zhao, Q. Liu, *Inorg. Chem. Front.* **2019**, *6*, 3621.
- [44] C. Liu, Z. Qi, C.-G. Ma, P. Dorenbos, D. Hou, S. Zhang, X. Kuang, J. Zhang, H. Liang, *Chem. Mater.* **2014**, *26*, 3709.
- [45] B. H. Toby, *J. Appl. Crystallogr.* **2001**, *34*, 210.
- [46] J. Hafner, *J. Comput. Chem.* **2008**, *29*, 2044.
- [47] G. Kresse, J. Furthmüller, *Phys. Rev. B* **1996**, *54*, 11169.
- [48] G. Kresse, J. Hafner, *Phys. Rev. B* **1993**, *47*, 558.
- [49] P. Hohenberg, W. Kohn, *Phys. Rev.* **1964**, *136*, B864.
- [50] J. Heyd, G. E. Scuseria, M. Ernzerhof, *J. Chem. Phys.* **2003**, *118*, 8207.
- [51] L. Yao, Q. Shao, S. Han, C. Liang, J. He, J. Jiang, *Chem. Mater.* **2020**, *32*, 2430.
- [52] H. Wu, L. Jiang, K. Li, C. Li, H. Zhang, *J. Mater. Chem. C* **2021**, *9*, 11761.
- [53] D. Hou, H. Lin, Y. Zhang, J. Y. Li, H. Li, J. Dong, Z. Lin, R. Huang, *Inorg. Chem. Front.* **2021**, *8*, 2333.